RESEARCH ARTICLE
SPACE PHYSICS: MAGNETOSPHERIC PHYSICS

Earth and Planetary Physics
7: 436–444, 2023
doi: 10.26464/epp2023043

The effect of the guide field on energy conversion during collisionless magnetic reconnection

Hui Xiao[1,2], ZhiHong Zhong[1,2*], Meng Zhou[1,2*], YongYuan Yi[1,2], LiangJin Song[2,3], Ye Pang[1,2], and XiaoHua Deng[1,2,3]

[1]School of Physics and Materials Science, Nanchang University, Nanchang 330031, China;

[2]Institute of Space Science and Technology, Nanchang University, Nanchang 330031, China;

[3]School of Resources and Environment, Nanchang University, Nanchang 330031, China

Key Points:

- The overall energy conversion first decreases steeply and then increases slowly when the guide field increases from $B_g = 0$ to $B_g = 4$.
- The overall energy conversion is predominantly contributed by $\boldsymbol{J}_\perp \cdot \boldsymbol{E}_\perp$ rather than $J_\parallel E_\parallel$ at any of the guide fields.
- The contribution from the fore reconnection front becomes important when $3 < B_g \leq 4$ because of the enhanced electron energy gain.

Citation: Xiao, H., Zhong, Z. H., Zhou, M., Yi, Y. Y., Song, L. J., Pang, Y., and Deng, X. H. (2023). The effect of the guide field on energy conversion during collisionless magnetic reconnection. *Earth Planet. Phys.*, *7*(4), 436–444. http://doi.org/10.26464/epp2023043

Abstract: Magnetic reconnection is well known as an efficient mechanism for transferring magnetic energy into plasma energy. However, how the energy conversion and partition between different species is influenced by the shear angle of the reconnecting magnetic component (i.e., the guide field strength) is not well understood. Using 2.5-dimensional particle-in-cell simulations, we investigated the energy conversion in reconnection with different guide fields. We found that the overall energy conversion first decreases steeply and then increases slowly when the guide field increases from $B_g = 0$ to $B_g = 4$. The increase in energy conversion in the large guide field regime is due to the electron energy gain through the perpendicular channel $\boldsymbol{J}_\perp \cdot \boldsymbol{E}_\perp$. The overall energy conversion is predominantly contributed by $\boldsymbol{J}_\perp \cdot \boldsymbol{E}_\perp$ rather than $J_\parallel E_\parallel$. We further find that energy conversion mainly occurs within the reconnection front and the flux pileup region. However, the contribution from the fore reconnection front becomes important in large guide field regimes ($3 < B_g \leq 4$) because of the enhanced electron energy gain.

Keywords: collisionless magnetic reconnection; energy conversion; guide field; particle-in-cell simulation

1. Introduction

Magnetic reconnection, which rapidly transfers magnetic energy into the kinetic and thermal energy of plasmas, is a ubiquitous and fundamental physical process in various kinds of magnetized plasma systems, such as black hole magnetospheres, solar coronas, tokamaks, and planetary magnetospheres (Parker, 1957; Hoshino et al., 2001; Drake et al., 2006; Yamada et al., 2010; Huang SY et al., 2015; Zhou M et al., 2017; Zong QG and Zhang H, 2018; Hesse and Cassak, 2020; Huang HT et al., 2021; Lu QM et al., 2022). It is considered the source of many explosive phenomena in these regions, such as stellar flares (Masuda et al., 1994; Krucker et al., 2010; Lin RP, 2011), coronal mass ejections (e.g., Chen PF and Shibata, 2000), and planetary storms and substorms (Russell and McPherron, 1973; Perreault and Akasofu, 1978; Øieroset et al., 2002). Energy conversion is one of the fundamental features of magnetic reconnection. How the efficiency of energy conversion varies in response to different ambient plasma and magnetic parameters is an important open question.

The guide field is a uniform magnetic field along the out-of-plane direction in reconnection. Its magnitude can change in a very broad range. For example, Burch et al. (2016) and Torbert et al. (2018) observed an anti-parallel magnetic reconnection in Earth's magnetosphere (guide field $B_g \sim 0$), whereas Eriksson et al. (2016) reported a magnetic reconnection with a large guide field $B_g \sim 4B_0$ at the magnetopause, where B_0 is the asymptotic magnetic field of reconnection. The guide field has been considered to substantially modify the dynamics and configuration of reconnection, such as the structures of the Hall electromagnetic field and the diffusion region (Pritchett, 2001; Ricci et al., 2004; Fu XR et al., 2006; Eastwood et al., 2010; Huang C et al., 2010; Lu S et al., 2011; Wang RS et al., 2012; Fu S et al., 2018; Zhou M et al., 2019; Zhong ZH et al., 2020a, 2022). Furthermore, the guide field is believed to be one of the key factors in effectively modulating energy conversion in reconnection (Shu YK et al., 2021, 2022; Sang LL et al., 2022).

The influence of the guide field on energy conversion during reconnection has been investigated through laboratory experiments, numerical simulations, and satellite observations. Ono et al. (2012) noted in their spheromak merging experiment that the

First author: H. Xiao, huixiao.2023@gmail.com
Correspondence to: Z. H. Zhong, zhong.zh@outlook.com
M. Zhou, monmentum82@gmail.com
Received 17 FEB 2023; Accepted 17 APR 2023.
Accepted article online 26 MAY 2023.

extent of ion heating depended on the strength of the guide field. Tanabe et al. (2015) found that a toroidal guide field mostly contributes to the formation of a peaked electron heating profile at the X-point and that localized heating increases with an increase in the guide field on the Mega-Ampere Spherical Tokamak (MAST). Using magnetospheric multiscale (MMS) measurements, Genestreti et al. (2017) showed that increasing the guide field strength appears to move local energy conversion from the electron-crescent point to the X-point in asymmetric reconnection. Fox et al. (2018) demonstrated that $\boldsymbol{J}\cdot\boldsymbol{E}$ near the X-line is dominated by $J_{\parallel}E_{\parallel}$ during guide field reconnection in both scaled laboratory and space experiments. At present, a common understanding of the energy conversion in the vicinity of the X-line is that $\boldsymbol{J}\cdot\boldsymbol{E}$ is primarily contributed by the perpendicular current and electric field (i.e., $\boldsymbol{J}_{\perp}\cdot\boldsymbol{E}_{\perp}$) in a weak guide field regime, whereas $\boldsymbol{J}\cdot\boldsymbol{E}$ is mainly contributed by $J_{\parallel}E_{\parallel}$ when the guide field is relatively large. Pucci et al. (2018) found via simulation that the transition from $\boldsymbol{J}_{\perp}\cdot\boldsymbol{E}_{\perp}$ to $J_{\parallel}E_{\parallel}$ happens around $B_g = 0.6$, whereas Wilder et al. (2018) showed by MMS observations that the transition value should be smaller than $B_g = 0.5$. Energy conversion is widely accepted to occur not only near the X-line region but also in the outflow region, such as the reconnection front (Khotyaintsev et al., 2016; Zhong ZH et al., 2019; Huang J et al., 2019), the magnetic flux rope (Lapenta et al., 2014; Sitnov et al., 2014; Huang C et al., 2015; Zhu BJ et al., 2019; Zhong ZH et al., 2020b), or the secondary reconnection sites (Zhou M et al., 2012). Therefore, an investigation of the energy budget of reconnection should not consider only the X-line region. Recent simulations suggest that both the reconnection rate and the energy conversion rate $\boldsymbol{J}\cdot\boldsymbol{E}$ integrated over the reconnection region (including both the X-line and the outflow region) are reduced as the guide field increases from $B_g = 0$ to $B_g = 2$ (Werner and Uzdensky, 2017; Yi YY et al., 2019). However, many details about how the guide field affects energy conversion in the reconnection are unknown.

In this work, we conducted a series of 2.5-dimensional (2.5-D) particle-in-cell (PIC) simulations to study the effect of the guide field on energy conversion in collisionless symmetric reconnection. In Section 2 of this article, we introduce the simulation model and the initial parameters of reconnection. In Section 3.1, we present the features of energy conversion in the entire reconnection plane under different guide fields. In Section 3.2, we present the variation in the integrated $J_{\parallel}E_{\parallel}$ and $\boldsymbol{J}_{\perp}\cdot\boldsymbol{E}_{\perp}$ as a function of different guide fields. In Section 3.3, we show the energy conversion in different subregions of reconnection under different guide fields. Discussion and summaries are given in Section 4.

2. Simulation Model

We carried out the simulations using a 2.5-D fully electromagnetic PIC code that has frequently been used to study collisionless reconnection (Zhou M et al., 2012, 2014; Huang C et al., 2014; Song LJ et al., 2019; Yi YY et al., 2019; Zhong ZH et al., 2021). The initial equilibrium configuration is given by the Harris equilibrium, $B_x = B_0\tanh(z/L_0)$, where B_0 is the asymptotic magnetic field and L_0 is the half-width of the initial current sheet. A series of simulations with different guide fields (cases 1–9 in Table 1) were performed. The domain size of these simulations is $L_x \times L_z = 60d_{\rm i} \times 30d_{\rm i}$, discretized by 2,400 × 1,200 cells, where $d_{\rm i} = c/\omega_{\rm pi}$, c is the speed of light, and $\omega_{\rm pi} = (n_0q^2/m_{\rm i}\epsilon_0)^{1/2}$ is the ion plasma frequency. The other simulation parameters are as follows: the mass ratio $m_{\rm i}/m_{\rm e} = 100$, $L_0 = 0.5d_{\rm i}$, $T_{\rm i}/T_{\rm e} = 4$, and $\omega_{\rm pe}/\omega_{\rm ce} = 2$. In addition, we performed case 10 with an extremely large guide field $B_g = 10$, and we performed case 11 with a zero guide field but with $T_{\rm i}/T_{\rm e} = 1$. The reconnection occurs in the X–Z plane in these simulations. Periodic boundary conditions are applied in the X and Y directions, and the ideal conducting boundary conditions are applied in the Z direction.

All physical quantities are normalized as follows. The magnetic field is normalized by the asymptotic magnetic field B_0. The electric field is normalized by $v_{\rm A}B_0$, where $v_{\rm A}$ is the Alfvén speed calculated by B_0 and the density n_0 at the center of the current sheet. Lengths are normalized by ion inertia length $d_{\rm i}$ based on n_0. Time is normalized by the inverse ion cyclotron frequency $\Omega_{\rm i}^{-1}$. The energy conversion rate is normalized by $qn_0v_{\rm A}^2B_0d_{\rm i}^2$.

3. Simulation Results

3.1 Overall Energy Conversion Rate

Reconnection occurs in the center ($Z = 0$) of the X–Z plane in these simulations because of the initially imposed perturbation. Figure 1a shows the variation in the reconnection rate as a function of time under different guide fields. The reconnection rate is calculated by $E_{\rm r} = \partial\psi/\partial t$, where $\psi = \max(A_y) - \min(A_y)$ along $Z = 0$ and A_y is the Y component of the magnetic vector potential. We can see that the peaks in the reconnection rate decrease as the B_g increases. When the guide field is greater than 2, it has little influence on the peak reconnection rate, as shown by the blue, green, magenta, and cyan curves in Figure 1a. In contrast, the reconnection rate becomes very small when $B_g = 10$ (yellow curve). Additionally, we found that the reconnection rate fluctuates significantly in the later stages of case 3 with $B_g = 1$, after the rapid formation and annihilation of small-scale secondary magnetic islands in or near the X-line region. A similar fluctuation in the reconnection rate can also be observed in case 4 with $B_g = 1.5$ (not shown). Figure 1b shows the temporal evolution of the integrated energy conversion rate $\int \boldsymbol{J}\cdot\boldsymbol{E}{\rm d}s$ as a function of the guide fields. The end time of each curve in Figure 1b is the time when $\int \boldsymbol{J}\cdot\boldsymbol{E}{\rm d}s$ reaches its peak, which is also the time when the two outflows encounter each other because of the periodic boundary conditions

Table 1. The guide field strength B_g and the ratio between ion and electron temperature $T_{\rm i}/T_{\rm e}$ of the simulations performed.

	Case										
	1	2	3	4	5	6	7	8	9	10	11
$\frac{T_{\rm i}}{T_{\rm e}}$	4	4	4	4	4	4	4	4	4	4	1
B_g	0	0.5	1.0	1.5	2.0	2.5	3.0	3.5	4.0	10.0	0

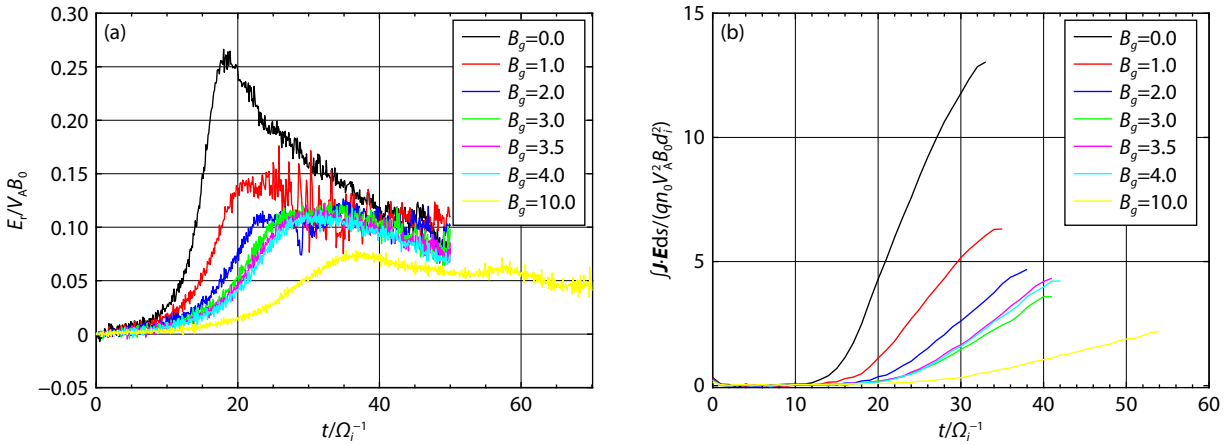

Figure 1. Reconnection rate and energy conversion rate. (a) Temporal evolution of the reconnection rate for different guide fields. (b) Temporal evolution of the integrated energy conversion rate $\int \boldsymbol{J}\cdot\boldsymbol{E}ds$ over the entire simulation region as a function of the guide fields.

in the X direction (Yi YY et al., 2019). Therefore, we considered the energy conversion process before the peak of $\int \boldsymbol{J}\cdot\boldsymbol{E}ds$ in the following analysis. We found that $\int \boldsymbol{J}\cdot\boldsymbol{E}ds$ generally declines as B_g increases; however, case 8 (B_g = 3.5, magenta curve in Figure 1b) and case 9 (B_g = 4, cyan curve in Figure 1b) present the reverse trend. The $\int \boldsymbol{J}\cdot\boldsymbol{E}ds$ in cases 8 and 9 is slightly larger than that in case 7 (B_g = 3, green curve in Figure 1b).

Because $\boldsymbol{J}\cdot\boldsymbol{E} = \boldsymbol{J}_i\cdot\boldsymbol{E} + \boldsymbol{J}_e\cdot\boldsymbol{E}$, we evaluated the contribution of ion energy gain $\boldsymbol{J}_i\cdot\boldsymbol{E}$ and electron energy gain $\boldsymbol{J}_e\cdot\boldsymbol{E}$ to $\boldsymbol{J}\cdot\boldsymbol{E}$, respectively. Figure 2 displays the spatial distribution of $\boldsymbol{J}\cdot\boldsymbol{E}$, $\boldsymbol{J}_i\cdot\boldsymbol{E}$, and $\boldsymbol{J}_e\cdot\boldsymbol{E}$ in the reconnection plane for the case with B_g = 0 (Figures 2a–c) and for the case with B_g = 4 (Figures 2d–f). In both cases, intense $\boldsymbol{J}\cdot\boldsymbol{E}$ mainly occurs in the X-line region and the outflow region, as shown in Figures 2a, d. Small-scale structures with oscillating $\boldsymbol{J}\cdot\boldsymbol{E}$ (positive and negative values) are abundant in the fore reconnection front region in the case of the large guide field (Figure 2d). Yi et al. (2023) reported these structures as turbulence in this region. Figures 2b, e show that intense $\boldsymbol{J}_i\cdot\boldsymbol{E}$ is mainly in the outflow region because the ions have a large bulk velocity in the outflow. An intense $\boldsymbol{J}_e\cdot\boldsymbol{E}$ occurs in both the X-line region, where electrons are accelerated by the reconnection electric field, and

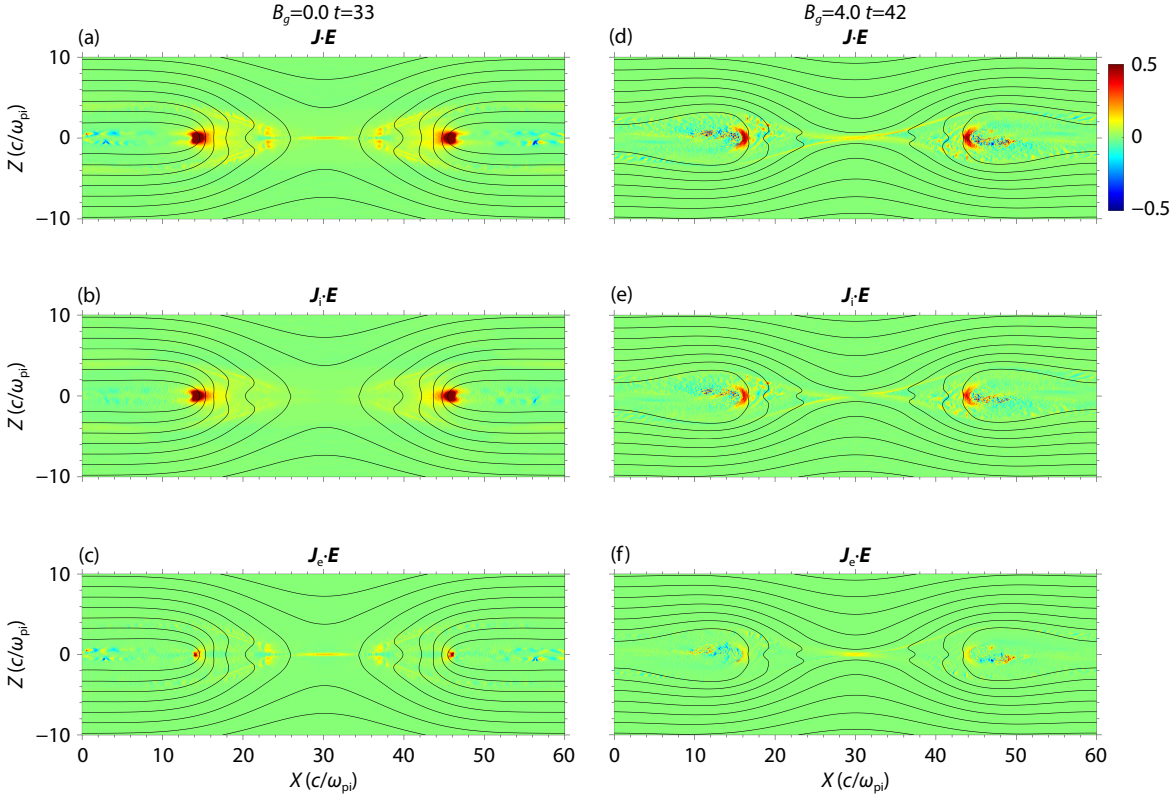

Figure 2. Spatial distributions of $\boldsymbol{J}\cdot\boldsymbol{E}$, $\boldsymbol{J}_i\cdot\boldsymbol{E}$, $\boldsymbol{J}_e\cdot\boldsymbol{E}$. (a–c) $\boldsymbol{J}\cdot\boldsymbol{E}$, $\boldsymbol{J}_i\cdot\boldsymbol{E}$, and $\boldsymbol{J}_e\cdot\boldsymbol{E}$ at t = 33 in the case of B_g = 0, respectively. (d–f) $\boldsymbol{J}\cdot\boldsymbol{E}$, $\boldsymbol{J}_i\cdot\boldsymbol{E}$, and $\boldsymbol{J}_e\cdot\boldsymbol{E}$ at t = 42 in the case of B_g = 4, respectively. Black curves represent the in-plane magnetic field lines.

the outflow region (Figures 2c, f).

In observations of space plasma, the guide fields of most magnetic reconnection events are below 4. Next, we focused on the energy conversion during B_g = [0, 4]. We integrated the $\boldsymbol{J}\cdot\boldsymbol{E}$ over space and time, denoted as $\iint \boldsymbol{J}\cdot\boldsymbol{E}\mathrm{d}s\mathrm{d}t$ to examine the accumulated energy conversion from t = 0 to $t = t_p$ when $\int \boldsymbol{J}\cdot\boldsymbol{E}\mathrm{d}s$ reaches its peak (Figure 1b). Figure 3a displays $\iint \boldsymbol{J}\cdot\boldsymbol{E}\mathrm{d}s\mathrm{d}t$, $\iint \boldsymbol{J}_\mathrm{i}\cdot\boldsymbol{E}\mathrm{d}s\mathrm{d}t$, and $\iint \boldsymbol{J}_\mathrm{e}\cdot\boldsymbol{E}\mathrm{d}s\mathrm{d}t$ in cases 1–9. We saw that the accumulated energy release (black curve in Figure 3a) steeply decreases as the guide field increases from B_g = 0 to B_g = 2.5, whereas it increases as B_g increases from 3 to 4. Although there is a small increase in $\iint \boldsymbol{J}_\mathrm{i}\cdot\boldsymbol{E}\mathrm{d}s\mathrm{d}t$ as the guide field changes from 2.5 to 3, the overall trend of $\iint \boldsymbol{J}_\mathrm{i}\cdot\boldsymbol{E}\mathrm{d}s\mathrm{d}t$ (blue curve in Figure 3a) is that it decreases with the enhancement of the guide field. Expression $\iint \boldsymbol{J}_\mathrm{e}\cdot\boldsymbol{E}\mathrm{d}s\mathrm{d}t$ slightly declines with increasing B_g when $B_g < 3$ and increases sharply when $B_g > 3$ (red curve in Figure 3a). These results imply that the enhancement of the electron energy gain leads to an increase in the total energy conversion when $B_g > 3$. Figure 3b shows the ratio of $\iint \boldsymbol{J}_\mathrm{i}\cdot\boldsymbol{E}\mathrm{d}s\mathrm{d}t$ over $\iint \boldsymbol{J}\cdot\boldsymbol{E}\mathrm{d}s\mathrm{d}t$, and $\iint \boldsymbol{J}_\mathrm{e}\cdot\boldsymbol{E}\mathrm{d}s\mathrm{d}t$ over $\iint \boldsymbol{J}\cdot\boldsymbol{E}\mathrm{d}s\mathrm{d}t$ for different cases. The $\iint \boldsymbol{J}_\mathrm{e}\cdot\boldsymbol{E}\mathrm{d}s\mathrm{d}t/\iint \boldsymbol{J}\cdot\boldsymbol{E}\mathrm{d}s\mathrm{d}t$ (red curve) slowly increases as B_g changes from 0 to 2, then decreases as B_g changes from 2 to 3, and it shows a steep enhancement when the guide field increases from 3 to 4. The electrons gain approximately 16% of the released energy when B_g = 0, and they gain approximately 40% of the released energy when B_g = 4. The enhanced proportion of the electron energy gain when $B_g > 3$ (Figure 3b) is caused by both the reduction in the ion energy gain and the enhancement of the electron energy gain (Figure 3a).

3.2 Energy Conversion Through the Parallel and Perpendicular Channels

To reveal the relative importance of the parallel and perpendicular electric fields (with respect to the ambient magnetic field) in energy conversion for different guide fields, we decomposed $\boldsymbol{J}\cdot\boldsymbol{E}$ into the parallel channel $J_\parallel E_\parallel$ and the perpendicular channel $\boldsymbol{J}_\perp\cdot\boldsymbol{E}_\perp$. Figure 4a displays the accumulated $\iint J_\parallel E_\parallel \mathrm{d}s\mathrm{d}t$ and $\iint \boldsymbol{J}_\perp\cdot\boldsymbol{E}_\perp\mathrm{d}s\mathrm{d}t$ as a function of the guide field. One can see that $\iint \boldsymbol{J}_\perp\cdot\boldsymbol{E}_\perp\mathrm{d}s\mathrm{d}t$ is much larger than $\iint J_\parallel E_\parallel\mathrm{d}s\mathrm{d}t$ and is the dominant contribution to $\iint \boldsymbol{J}\cdot\boldsymbol{E}\mathrm{d}s\mathrm{d}t$ for all the cases. The increase in $\iint \boldsymbol{J}\cdot\boldsymbol{E}\mathrm{d}s\mathrm{d}t$ when $B_g > 3$ is caused by the enhancement of $\iint \boldsymbol{J}_\perp\cdot\boldsymbol{E}_\perp\mathrm{d}s\mathrm{d}t$ rather than $\iint J_\parallel E_\parallel\mathrm{d}s\mathrm{d}t$. Figure 4b shows $\iint \boldsymbol{J}_\perp\cdot\boldsymbol{E}_\perp\mathrm{d}s\mathrm{d}t/\iint \boldsymbol{J}\cdot\boldsymbol{E}\mathrm{d}s\mathrm{d}t$ and $\iint J_\parallel E_\parallel\mathrm{d}s\mathrm{d}t/\iint \boldsymbol{J}\cdot\boldsymbol{E}\mathrm{d}s\mathrm{d}t$ as a function of the guide fields. The $\iint \boldsymbol{J}_\perp\cdot\boldsymbol{E}_\perp\mathrm{d}s\mathrm{d}t/\iint \boldsymbol{J}\cdot\boldsymbol{E}\mathrm{d}s\mathrm{d}t$ is reduced slightly as B_g increases from 0 to 3 and is elevated as B_g changes from 3 to 4. The $\iint \boldsymbol{J}_\perp\cdot\boldsymbol{E}_\perp\mathrm{d}s\mathrm{d}t$ is always greater than 80% of the $\iint \boldsymbol{J}\cdot\boldsymbol{E}\mathrm{d}s\mathrm{d}t$.

The energy conversion through the perpendicular and parallel channels as a function of B_g for different species is presented in Figures 4c, d. For ions, both $\iint J_{\mathrm{i}\parallel}E_\parallel\mathrm{d}s\mathrm{d}t$ and $\iint \boldsymbol{J}_{\mathrm{i}\perp}\cdot\boldsymbol{E}_\perp\mathrm{d}s\mathrm{d}t$ decrease with the increase in the guide field. This means that the guide field suppresses the ion energy gain in both the perpendicular and parallel channels. Although the decrease in $\iint \boldsymbol{J}_{\mathrm{i}\perp}\cdot\boldsymbol{E}_\perp\mathrm{d}s\mathrm{d}t$ is steeper than that of $\iint J_{\mathrm{i}\parallel}E_\parallel\mathrm{d}s\mathrm{d}t$ (Figure 4c), ions still gain energy mainly through the perpendicular channel for all the guide fields we examined. Figure 4d illustrates that the electron energy gain through the parallel channel $\iint J_{\mathrm{e}\parallel}E_\parallel\mathrm{d}s\mathrm{d}t$ increases steeply when B_g increases from 0 to 1, then it maintains a relative constant level. In contrast, $\iint \boldsymbol{J}_{\mathrm{e}\perp}\cdot\boldsymbol{E}_\perp\mathrm{d}s\mathrm{d}t$ decreases sharply when B_g increases from 0 to 3, then it increases rapidly as B_g reaches 4. This indicates that the aforementioned enhancement of $\iint \boldsymbol{J}_\mathrm{e}\cdot\boldsymbol{E}\mathrm{d}s\mathrm{d}t$ when $B_g > 3$ is caused by the elevated electron energy gain through the perpendicular channel.

3.3 Energy Conversion in Different Regions

We divided the reconnection plane into four subregions: the X-line region (XLR), the flux pileup region (FPR), the reconnection front (RF), and the fore reconnection front (FRF) to illustrate the spatial distribution of the energy conversion during reconnection. As shown in Figure 5, P1, P2, and P3 are points on the line Z = 0. Point P1 indicates the location where the magnitude of $\boldsymbol{J}\cdot\boldsymbol{E}$ is 1/e (where e is Euler's number) of the peak $\boldsymbol{J}\cdot\boldsymbol{E}$ on Z = 0. Points P2 and P3 indicate the locations where B_z is 0.9 and 0.1 of the peak B_z on Z = 0, respectively. Magnetic field lines L1, L2, and L3 are the closed magnetic field lines (attributable to the periodic boundary condition) through P1, P2, and P3, respectively. The vertical dashed line L4 is the line through the point of the largest Z coordi-

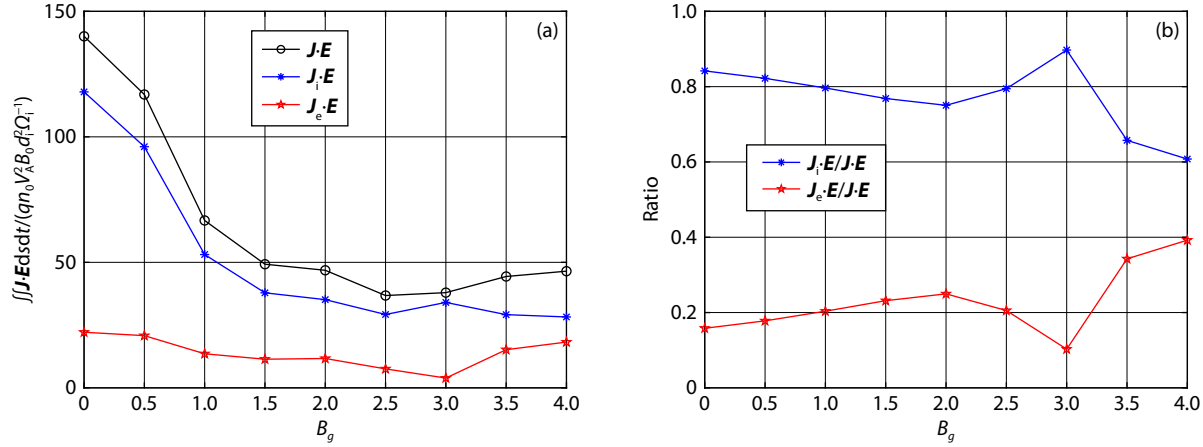

Figure 3. Entire energy conversion under different guide fields. (a) $\iint \boldsymbol{J}\cdot\boldsymbol{E}\mathrm{d}s\mathrm{d}t$, $\iint \boldsymbol{J}_\mathrm{i}\cdot\boldsymbol{E}\mathrm{d}s\mathrm{d}t$, and $\iint \boldsymbol{J}_\mathrm{e}\cdot\boldsymbol{E}\mathrm{d}s\mathrm{d}t$ as a function of the guide field. (b) $\iint \boldsymbol{J}_\mathrm{i}\cdot\boldsymbol{E}\mathrm{d}s\mathrm{d}t/\iint \boldsymbol{J}\cdot\boldsymbol{E}\mathrm{d}s\mathrm{d}t$ and $\iint \boldsymbol{J}_\mathrm{e}\cdot\boldsymbol{E}\mathrm{d}s\mathrm{d}t/\iint \boldsymbol{J}\cdot\boldsymbol{E}\mathrm{d}s\mathrm{d}t$ as a function of the guide field.

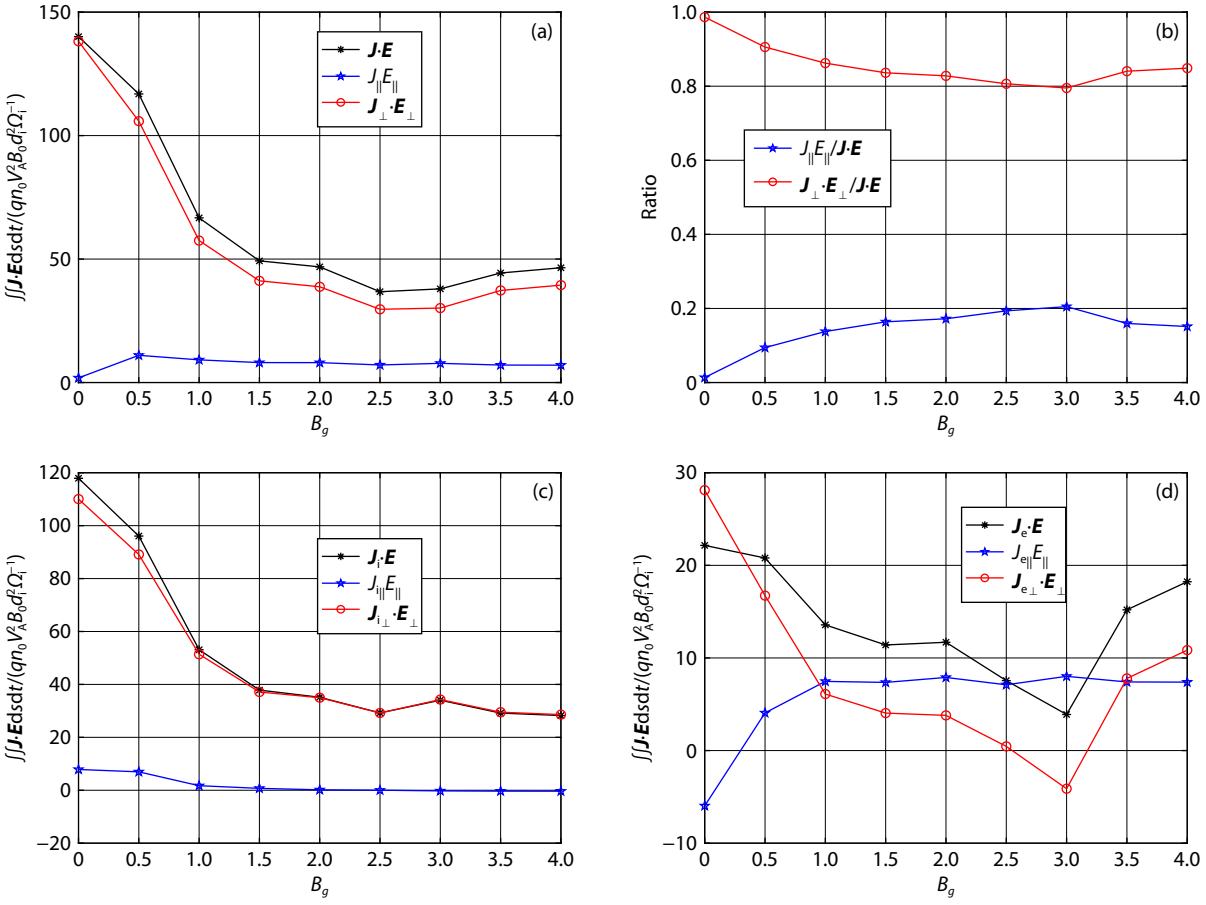

Figure 4. Energy conversion in the parallel and perpendicular channels under different guide fields. (a) $\iint J_{\parallel}E_{\parallel}\mathrm{d}s\mathrm{d}t$, $\iint \boldsymbol{J}_{\perp}\cdot\boldsymbol{E}_{\perp}\mathrm{d}s\mathrm{d}t$, and $\iint \boldsymbol{J}\cdot\boldsymbol{E}\mathrm{d}s\mathrm{d}t$ as a function of the guide field. (b) $\iint J_{\parallel}E_{\parallel}\mathrm{d}s\mathrm{d}t/\iint \boldsymbol{J}\cdot\boldsymbol{E}\mathrm{d}s\mathrm{d}t$ and $\iint \boldsymbol{J}_{\perp}\cdot\boldsymbol{E}_{\perp}\mathrm{d}s\mathrm{d}t/\iint \boldsymbol{J}\cdot\boldsymbol{E}\mathrm{d}s\mathrm{d}t$ as a function of the guide field. (c) $\iint J_{i\parallel}E_{\parallel}\mathrm{d}s\mathrm{d}t$, $\iint \boldsymbol{J}_{i\perp}\cdot\boldsymbol{E}_{\perp}\mathrm{d}s\mathrm{d}t$, and $\iint \boldsymbol{J}_i\cdot\boldsymbol{E}\mathrm{d}s\mathrm{d}t$ as a function of the guide field. (d) $\iint J_{e\parallel}E_{\parallel}\mathrm{d}s\mathrm{d}t$, $\iint \boldsymbol{J}_{e\perp}\cdot\boldsymbol{E}_{\perp}\mathrm{d}s\mathrm{d}t$, and $\iint \boldsymbol{J}_e\cdot\boldsymbol{E}\mathrm{d}s\mathrm{d}t$ as a function of the guide field.

nate on magnetic field line L3. The boundaries of the XLR in the X direction are determined by the two edge points of L1 in the X direction, whereas its boundaries in the Z direction are set at $Z = -1$ and $Z = 1$, respectively, as marked by the red rectangle in Figure 5. The area encircled by magnetic field lines L1, L2, and L4 near the XLR is defined as the FPR (marked by the yellow block). The area encircled by lines L2, L3, and L4 near the FPR is defined as the RF (marked by the blue area). The area encircled by closed magnetic field line L1 except for the yellow and blue areas is defined as the FRF, which is marked by the black shadow in Figure 5.

Figures 6a, b present the integrated $\boldsymbol{J}\cdot\boldsymbol{E}$ in different regions. It should be noted that the start time is not $t = 0$ because there is no reconnection and the consequent subregions at the beginning of the simulation. The time instant when $\boldsymbol{J}\cdot\boldsymbol{E}$ begins to rise (shown in Figure 1b) is used as the start time, which is also the start time for integration in calculating $\iint \boldsymbol{J}\cdot\boldsymbol{E}\mathrm{d}s\mathrm{d}t$, as shown in Figures 6c, d. The peak time of $\int \boldsymbol{J}\cdot\boldsymbol{E}\mathrm{d}s$ is used as the end time for integration. Figures 6a, b show the temporal evolution of the integrated $\boldsymbol{J}\cdot\boldsymbol{E}$ in different regions for case 1 ($B_g = 0$) and case 9 ($B_g = 4$), respectively. The black dotted curve is the sum of the spatial integrated $\boldsymbol{J}\cdot\boldsymbol{E}$ in the four regions, and the solid gray curve represents the integrated $\boldsymbol{J}\cdot\boldsymbol{E}$ in the entire simulation domain. The black dashed line is very close to the gray solid line (Figures 6a, b), indicating that the energy conversion occurs exclusively in these four regions. In both case 1 ($B_g = 0$) and case 9 ($B_g = 4$), energy conversion primarily occurs in the RF (red line) and the FPR (black line). Although $\boldsymbol{J}\cdot\boldsymbol{E}$ in the XLR is large (Figure 2d), the integrated $\boldsymbol{J}\cdot\boldsymbol{E}$ in the XLR (blue curves in Figures 6a, b) is much smaller than that in the RF and the FPR because the area of XLR is much smaller than that of the RF and FPR. Moreover, the integrated $\boldsymbol{J}\cdot\boldsymbol{E}$ in the FPR is larger than that in the RF for reconnection with $B_g = 0$ (Figure 6a), whereas the integrated $\boldsymbol{J}\cdot\boldsymbol{E}$ in the FPR is smaller than that in the RF under $B_g = 4$ (Figure 6b). The integrated $\boldsymbol{J}\cdot\boldsymbol{E}$ in the FRF (cyan curve in Figure 6b) is negative during the early stage of case 9 ($B_g = 4$). It later reverses to positive. This temporal evolution is not seen in case 1 ($B_g = 0$). These observations suggest that the guide field plays an important role in modulating the energy conversion in different regions of reconnection.

Figure 6c displays the variation in the temporal and spatial integrated energy conversion $\iint \boldsymbol{J}\cdot\boldsymbol{E}\mathrm{d}s\mathrm{d}t$ in each region as a function of the guide field strength. In the RF (denoted by the red curve), $\iint \boldsymbol{J}\cdot\boldsymbol{E}\mathrm{d}s\mathrm{d}t$ decreases as B_g increases from 0 to 2.5. It increases slowly as B_g increases from 2.5 to 4. In the FPR (black curve), the overall trend of $\iint \boldsymbol{J}\cdot\boldsymbol{E}\mathrm{d}s\mathrm{d}t$ decreases with the increase in the guide field. When $B_g < 1$, $\iint \boldsymbol{J}\cdot\boldsymbol{E}\mathrm{d}s\mathrm{d}t$ in the FPR is larger than that in

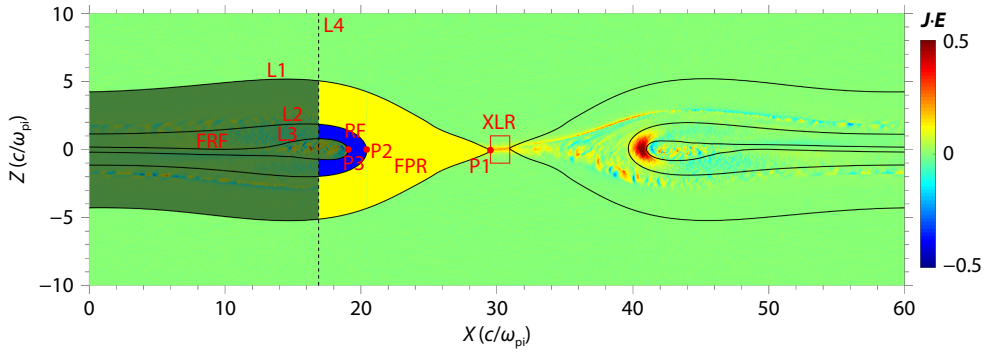

Figure 5. Schematic diagram of the four different regions in the reconnection plane: (1) the X-line region (XLR) marked by a red rectangle, (2) the flux pileup region (FPR) covered by the yellow shadow, (3) the reconnection front (RF) covered by the blue shadow, and (4) the fore reconnection front (FRF) covered by the black shadow. The same segmentation is used on the right side of the X-line as well. The color bar represents the magnitude of $\boldsymbol{J} \cdot \boldsymbol{E}$, and the black curves represent the in-plane magnetic field lines.

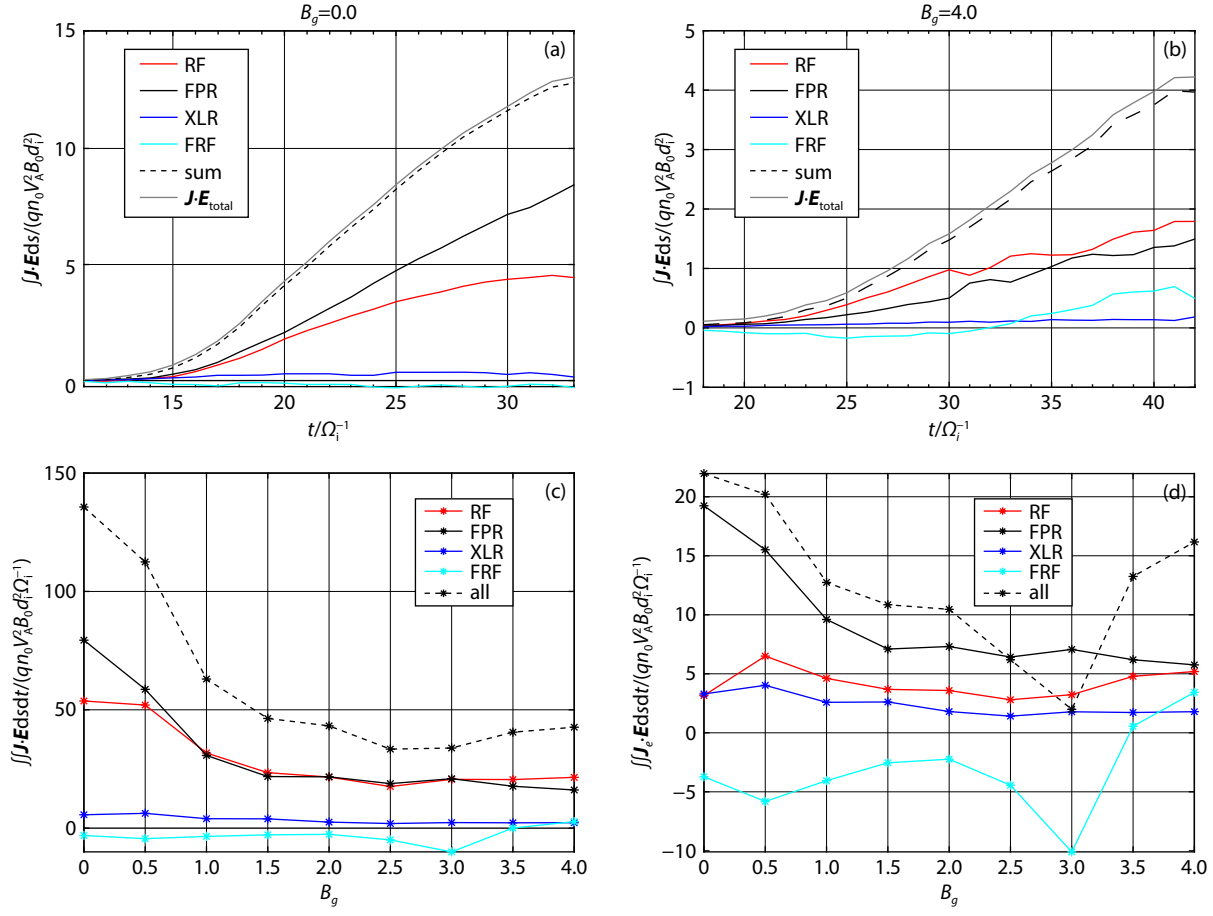

Figure 6. Energy conversion in different reconnection regions under different guide fields. (a, b) The energy conversion rate in different reconnection regions as a function of time in case 1 (B_g = 0) and case 9 (B_g = 4), respectively. (c) The entire energy conversion (integrated $\boldsymbol{J} \cdot \boldsymbol{E}$ over space and time) in different regions changed with guide fields. (d) The variation in the overall electron energy gain (integrated $\boldsymbol{J}_e \cdot \boldsymbol{E}$ over space and time) in different regions as a function of the guide field strength.

the RF. The $\iint \boldsymbol{J} \cdot \boldsymbol{E} \mathrm{d}s\mathrm{d}t$ in these two regions is comparable when $1 \le B_g \le 3$, and $\iint \boldsymbol{J} \cdot \boldsymbol{E} \mathrm{d}s\mathrm{d}t$ in the FPR is smaller than that in the RF when $B_g > 3$. Moreover, we can see that $\iint \boldsymbol{J} \cdot \boldsymbol{E} \mathrm{d}s\mathrm{d}t$ in the XLR (blue curve) decreases very slowly with the elevation of the guide field. The $\iint \boldsymbol{J} \cdot \boldsymbol{E} \mathrm{d}s\mathrm{d}t$ in the FRF (cyan curve) is negative when $B_g < 3.5$ and changes to positive when $B_g = 4$.

An interesting finding is that the electrons gain more energy with the increase of B_g when $B_g > 3$ (Figure 3a) because the electron energy gain is enhanced through the perpendicular channel (Figure 4d). Figure 6d presents the integrated energy gain of electrons in different regions. We see that the increase in $\boldsymbol{J}_e \cdot \boldsymbol{E}$ with increasing B_g when $B_g > 3$ (black dashed line) is mainly caused by

the enhancement of $\boldsymbol{J}_e \cdot \boldsymbol{E}$ in the FRF (cyan line). The electron energy gain at the FRF changes from negative to positive as the guide field increases from 3 to 4. This may be due to the small-scale oscillation of $\boldsymbol{J} \cdot \boldsymbol{E}$ in the FRF, which develops only in the large guide field regime, as shown in Figure 2d. A detailed study of the formation and evolution of these $\boldsymbol{J} \cdot \boldsymbol{E}$ oscillation structures is beyond the scope of this work and will be conducted in the future.

4. Discussion and Summary

Figure 3b illustrates that the percentage of ion and electron energy gain does not change monotonically as the guide field increases. We also performed two other cases (cases 10 and 11) to check the energy partition between ions and electrons. In case 10 with an extremely large guide field of $B_g = 10$, the electrons gain approximately 50% of the overall magnetic energy released, which is greater than that in case 9 (~40%, $B_g = 4$). This result implies that the guide field is an important factor in regulating the energy partition between ions and electrons. In case 11, we set the temperature ratio between ions and electrons as $T_i/T_e = 1$ and the guide field as $B_g = 0$. The electrons gain approximately 24% of the overall released magnetic energy in this case, which is greater than that in case 1 (~16%, $T_i/T_e = 4$, $B_g = 0$). This result implies that parameters other than the guide field also affect the energy partition. More investigations are required to reveal the law of energy partition in collisionless reconnection in the future.

In summary, the energy conversions in symmetric reconnection under different guide fields were investigated via 2.5-D PIC simulations. We explored the guide fields in the range of $0 \le B_g \le 4$, which almost covers the reconnection in different heliosphere regions available for *in situ* observations. Our study considers outflow regions and the X-line region as an integration; thus, it is an important supplement to previous studies that have focused only on the energy conversion in the vicinity of the X-line.

Our main results are summarized below:

(1) The reconnection rate decreases with the increase in the guide field, which is consistent with previous studies (e.g., Werner and Uzdensky, 2017; Yi YY et al., 2019). The integrated energy conversion in the entire simulation domain decreases with the elevation of the guide field until $B_g = 3$, after which it increases slightly with the enhancement of the guide field when $3 < B_g \le 4$.

(2) Although ions gain more energy than electrons for all the guide fields considered, ions gain less energy when the guide field is larger. The electron energy gain decreases with the increase in the guide field as well when $B_g < 3$, whereas it increases with the enhancement of the guide field and results in the enhancement of the overall energy conversion when $3 < B_g \le 4$.

(3) Ions gain energy primarily through the perpendicular channel (i.e., $\boldsymbol{J}_\perp \cdot \boldsymbol{E}_\perp$). The electron energy gain through the perpendicular channel decreases with the elevation of the guide field when $B_g < 3$ and increases with the elevation of the guide field when $3 < B_g \le 4$. The electron energy gain through the parallel channel increases with the enhancement of the guide field when $B_g < 1$. The gain in electron energy is insensitive to the guide field when $B_g > 1$. The gain is predominantly through the perpendicular channel when $B_g < 1$ and $B_g > 3.5$, whereas it is mainly from the parallel channel when $1 < B_g < 3.5$.

(4) Energy conversion occurs primarily in the FPR and RF for all the guide fields examined. In addition, the contribution from the FRF becomes important under a large guide field ($3 < B_g \le 4$) because of the enhanced electron energy gain through the perpendicular channel.

Acknowledgments

This work was supported by the National Natural Science Foundation of China (NSFC) under Grants 42074197, 42130211, 42104156, and 41774154 and the China Postdoctoral Science Foundation under Grant 2021M691395. The PIC simulations were performed on the supercomputers at Nanchang University.

References

Burch, J. L., Torbert, R. B., Phan, T. D., Chen, L. J., Moore, T. E., Ergun, R. E., Eastwood, J. P., Gershman, D. J., Cassak, P. A., ... Chandler, M. (2016). Electron-scale measurements of magnetic reconnection in space. *Science*, *352*(6290), aaf2939. https://doi.org/10.1126/science.aaf2939

Chen, P. F., and Shibata, K. (2000). An emerging flux trigger mechanism for coronal mass ejections. *Astrophys. J.*, *545*, 524–531. https://doi.org/10.1086/317803

Drake, J. F., Swisdak, M., Che, H., and Shay, M. A. (2006). Electron acceleration from contracting magnetic islands during reconnection. *Nature*, *443*(7111), 553–556. https://doi.org/10.1038/nature05116

Eastwood, J. P., Shay, M. A., Phan, T. D., and Øieroset, M. (2010). Asymmetry of the ion diffusion region hall electric and magnetic fields during guide field reconnection: observations and comparison with simulations. *Phys. Rev. Lett.*, *104*(20), 205001. https://doi.org/10.1103/PhysRevLett.104.205001

Eriksson, S., Wilder, F. D., Ergun, R. E., Schwartz, S. J., Cassak, P. A., Burch, J. L., Chen, L. J., Torbert, R. B., Phan, T. D., ... Marklund, G. T. (2016). Magnetospheric multiscale observations of the electron diffusion region of large guide field magnetic reconnection. *Phys. Rev. Lett.*, *117*(1), 015001. https://doi.org/10.1103/PhysRevLett.117.015001

Fox, W., Wilder, F. D., Eriksson, S., Jara-Almonte, J., Pucci, F., Yoo, J., Ji, H., Yamada, M., Ergun, R. E., ... Phan, T. D. (2018). Energy conversion by parallel electric fields during guide field reconnection in scaled laboratory and space experiments. *Geophys. Res. Lett.*, *45*(23), 12677–12684. https://doi.org/10.1029/2018gl079883

Fu, S., Huang, S. Y., Zhou, M., Ni, B. B., and Deng, X. H. (2018). Tripolar electric field structure in guide field magnetic reconnection. *Ann. Geophys.*, *36*(2), 373–379. https://doi.org/10.5194/angeo-36-373-2018

Fu, X. R., Lu, Q. M., and Wang, S. (2006). The process of electron acceleration during collisionless magnetic reconnection. *Phys. Plasmas*, *13*(1), 012309. https://doi.org/10.1063/1.2164808

Genestreti, K. J., Burch, J. L., Cassak, P. A., Torbert, R. B., Ergun, R. E., Varsani, A., Phan, T. D., Giles, B. L., Russell, C. T., ... Allen, R. C. (2017). The effect of a guide field on local energy conversion during asymmetric magnetic reconnection: MMS observations. *J. Geophys. Res.: Space Phys.*, *122*(11), 11342–11353. https://doi.org/10.1002/2017ja024247

Hesse, M., and Cassak, P. A. (2020). Magnetic reconnection in the space sciences: Past, present, and future. *J. Geophys. Res.: Space Phys.*, *125*(2), e2018JA025935. https://doi.org/10.1029/2018ja025935

Hoshino, M., Mukai, T., Terasawa, T., and Shinohara, I. (2001). Suprathermal electron acceleration in magnetic reconnection. *J. Geophys. Res.: Space Phys.*, *106*(A11), 25979–25997. https://doi.org/10.1029/2001ja900052

Huang, C., Lu, Q. M., and Wang, S. (2010). The mechanisms of electron acceleration in antiparallel and guide field magnetic reconnection. *Phys. Plasmas*, *17*(7), 072306. https://doi.org/10.1063/1.3457930

Huang, C., Lu, Q. M., Lu, S., Wang, P. R., and Wang, S. (2014). The effect of a guide field on the structures of magnetic islands formed during multiple X line reconnections: Two-dimensional particle-in-cell simulations. *J. Geophys. Res.*: *Space Phys.*, *119*(2), 798–807. https://doi.org/10.1002/2013ja019249

Huang, C., Wu, M. Y., Lu, Q. M., Wang, R. S., and Wang, S. (2015). Electron acceleration in the dipolarization front driven by magnetic reconnection. *J. Geophys. Res.*: *Space Phys.*, *120*(3), 1759–1765. https://doi.org/10.1002/2014ja020918

Huang, H. T., Yu, Y. Q., Cao, J. B., Dai, L., and Wang, R. S. (2021). On the ion distributions at the separatrices during symmetric magnetic reconnection. *Earth and Planetary Physics*, *5*(2), 205–217. https://doi.org/10.26464/epp2021019

Huang, J., Zhou, M., Li, H. M., Deng, X. H., Liu, J., and Huang, S. Y. (2019). Small-scale dipolarization fronts in the Earth's magnetotail. *Earth and Planetary Physics*, 3(4): 358–364. https://doi.org/10.26464/epp2019036

Huang, S. Y., Fu, H. S., Yuan, Z. G., Zhou, M., Fu, S., Deng, X. H., Sun, W. J., Pang, Y., Wang, D. D., ... Yu, X. D. (2015). Electromagnetic energy conversion at dipolarization fronts: Multispacecraft results. *J. Geophys. Res.*: *Space Phys.*, *120*(6), 4496–4502. https://doi.org/10.1002/2015ja021083

Khotyaintsev, Y. V., Graham, D. B., Norgren, C., Eriksson, E., Li, W., Johlander, A., Vaivads, A., André, M., Pritchett, P. L., ... Burch, J. L. (2016). Electron jet of asymmetric reconnection. *Geophys. Res. Lett.*, *43*(11), 5571–5580. https://doi.org/10.1002/2016gl069064

Krucker, S., Hudson, H. S., Glesener, L., White, S. M., Masuda, S., Wuelser, J. P., and Lin, R. P. (2010). Measurements of the coronal acceleration region of a solar flare. *Astrophys. J.*, *714*(2), 1108–1119. https://doi.org/10.1088/0004-637x/714/2/1108

Lapenta, G., Goldman, M., Newman, D., Markidis, S., and Divin, A. (2014). Electromagnetic energy conversion in downstream fronts from three dimensional kinetic reconnection. *Phys. Plasmas*, *21*(5), 055702. https://doi.org/10.1063/1.4872028

Lin, R. P. (2011). Energy release and particle acceleration in flares: Summary and future prospects. *Space Sci. Rev.*, *159*(1–4), 421–445. https://doi.org/10.1007/s11214-011-9801-0

Lu, Q. M., Fu, H. S., Wang, R. S., and Lu, S. (2022). Collisionless magnetic reconnection in the magnetosphere. *Chinese Phys. B*, *31*(8), 089401. https://doi.org/10.1088/1674-1056/ac76ab

Lu, S., Lu, Q. M., Cao, Y., Huang, C., Xie, J. L., and Wang, S. (2011). The effects of the guide field on the structures of electron density depletions in collisionless magnetic reconnection. *Chinese Sci. Bull.*, *56*(1), 48–52. https://doi.org/10.1007/s11434-010-4250-9

Masuda, S., Kosugi, T., Hara, H., Tsuneta, S., and Ogawara, Y. (1994). A loop-top hard x-ray source in a compact solar flare as evidence for magnetic reconnection. *Nature*, *371*(6497), 495–497. https://doi.org/10.1038/371495a0

Øieroset, M., Lin, R. P., Phan, T. D., Larson, D. E., and Bale, S. D. (2002). Evidence for electron acceleration up to ~300 keV in the magnetic reconnection diffusion region of Earth's magnetotail. *Phys. Rev. Lett.*, *89*(19), 195001. https://doi.org/10.1103/PhysRevLett.89.195001

Ono, Y., Tanabe, H., Yamada, T., Inomoto, M., Ii, T., Inoue, S., Gi, K., Watanabe, T., Gryaznevich, M., ... Cheng, C. Z. (2012). Ion and electron heating characteristics of magnetic reconnection in tokamak plasma merging experiments. *Plasma Phys. Control. Fusion*, *54*(12), 124039. https://doi.org/10.1088/0741-3335/54/12/124039

Parker, E. N. (1957). Sweet's mechanism for merging magnetic fields in conducting fluids. *J. Geophys. Res.*, *62*(4), 509–520. https://doi.org/10.1029/JZ062i004p00509

Perreault, P., and Akasofu, S. I. (1978). A study of geomagnetic storms. *Geophys. J. Int.*, *54*(3), 547–573. https://doi.org/10.1111/j.1365-246X.1978.tb05494.x

Pritchett, P. L. (2001). Geospace Environment Modeling magnetic reconnection challenge: Simulations with a full particle electromagnetic code. *J. Geophys. Res.*: *Space Phys.*, *106*(A3), 3783–3798. https://doi.org/10.1029/1999ja001006

Pucci, F., Usami, S., Ji, H., Guo, X., Horiuchi, R., Okamura, S., Fox, W., Jara-Almonte, J., Yamada, M., and Yoo, J. (2018). Energy transfer and electron energization in collisionless magnetic reconnection for different guide-field intensities. *Phys. Plasmas*, *25*(12), 122111. https://doi.org/10.1063/1.5050992

Ricci, P., Brackbill, J. U., Daughton, W., and Lapenta, G. (2004). Collisionless magnetic reconnection in the presence of a guide field. *Phys. Plasmas*, *11*(8), 4102–4114. https://doi.org/10.1063/1.1768552

Russell, C. T., and McPherron, R. L. (1973). The magnetotail and substorms. *Space. Sci. Rev.*, *15*(2), 205–266. https://doi.org/10.1007/BF00169321

Sang, L. L., Lu, Q. M., Xie, J. L., Fan, F. B., Zhang, Q. F., Ding, W. X., Zheng, J., and Sun, X. (2022). Energy dissipation during magnetic reconnection in the Keda linear magnetized plasma device. *Phys. Plasmas*, *29*(10), 102108. https://doi.org/10.1063/5.0090790

Shu, Y. K., Lu, S., Lu, Q. M., Ding, W. X., and Wang, S. (2021). Energy budgets from collisionless magnetic reconnection site to reconnection front. *J. Geophys. Res.*: *Space Phys.*, *126*(10), e2021JA029712. https://doi.org/10.1029/2021ja029712

Shu, Y. K., Lu, S., Lu, Q. M., Wang, R. S., Zheng, J., and Ding, W. X. (2022). Effects of guide field and background density and temperature on energy conversion at magnetic reconnection front. *J. Geophys. Res.*: *Space Phys.*, *127*(9), e2022JA030546. https://doi.org/10.1029/2022ja030546

Sitnov, M. I., Merkin, V. G., Swisdak, M., Motoba, T., Buzulukova, N., Moore, T. E., Mauk, B. H., and Ohtani, S. (2014). Magnetic reconnection, buoyancy, and flapping motions in magnetotail explosions. *J. Geophys. Res.*: *Space Phys.*, *119*(9), 7151–7168. https://doi.org/10.1002/2014ja020205

Song, L. J., Zhou, M., Yi, Y. Y., Deng, X. H., and Zhong, Z. H. (2019). Reconnection front associated with asymmetric magnetic reconnection: Particle-in-cell simulations. *Astrophys. J.*, *881*(1), L22. https://doi.org/10.3847/2041-8213/ab3655

Tanabe, H., Yamada, T., Watanabe, T., Gi, K., Kadowaki, K., Inomoto, M., Imazawa, R., Gryaznevich, M., Michael, C., ... The MAST Team. (2015). Electron and ion heating characteristics during magnetic reconnection in the MAST spherical tokamak. *Phys. Rev. Lett.*, *115*(21), 215004. https://doi.org/10.1103/PhysRevLett.115.215004

Torbert, R. B., Burch, J. L., Phan, T. D., Hesse, M., Argall, M. R., Shuster, J., Ergun, R. E., Alm, L., Nakamura, R., ... Saito, Y. (2018). Electron-scale dynamics of the diffusion region during symmetric magnetic reconnection in space. *Science*, *362*(6421), 1391–1395. https://doi.org/10.1126/science.aat2998

Wang, R. S., Nakamura, R., Lu, Q. M., Du, A. M., Zhang, T. L., Baumjohann, W., Khotyaintsev, Y. V., Volwerk, M., André, M., ... Lu, S. (2012). Asymmetry in the current sheet and secondary magnetic flux ropes during guide field magnetic reconnection. *J. Geophys. Res.*: *Space Phys.*, *117*(A7), A07223. https://doi.org/10.1029/2011ja017384

Werner, G. R., and Uzdensky, D. A. (2017). Nonthermal particle acceleration in 3D relativistic magnetic reconnection in pair plasma. *Astrophys. J.*, *843*(2), L27. https://doi.org/10.3847/2041-8213/aa7892

Wilder, F. D., Ergun, R. E., Burch, J. L., Ahmadi, N., Eriksson, S., Phan, T. D., Goodrich, K. A., Shuster, J., Rager, A. C., ... Khotyaintsev, Y. V. (2018). The role of the parallel electric field in electron-scale dissipation at reconnecting currents in the Magnetosheath. *J. Geophys. Res.*: *Space Phys.*, *123*(8), 6533–6547. https://doi.org/10.1029/2018ja025529

Yamada, M., Kulsrud, R., and Ji, H. T. (2010). Magnetic reconnection. *Rev. Mod. Phys.*, *82*(1), 603–664. https://doi.org/10.1103/RevModPhys.82.603

Yi, Y. Y., Zhou, M., Song, L. J., and Deng, X. H. (2019). On the energy conversion rate during collisionless magnetic reconnection. *Astrophys. J.*, *883*(1), L22. https://doi.org/10.3847/2041-8213/ab40c1

Yi, Y. Y., Pang, Y., Song, L. J., Jin, R. Q., and Deng, X. H. (2023). Particle-in-cell simulation of energy conversion at the turbulent region downstream of the reconnection front. *Astrophys. J.*, *946*(2), 112. https://doi.org/10.3847/1538-4357/acba19

Zhong, Z. H., Deng, X. H., Zhou, M., Ma, W. Q., Tang, R. X., Khotyaintsev, Y. V., Giles, B. L., Russell, C. T., and Burch, J. L. (2019). Energy conversion and dissipation at dipolarization fronts: A statistical overview. *Geophys. Res. Lett.*, *46*(22), 12693–12701. https://doi.org/10.1029/2019gl085409

Zhong, Z. H., Zhou, M., Tang, R. X., Deng, X. H., Khotyaintsev, Y. V., Giles, B. L., Paterson, W. R., Pang, Y., Man, H. Y., ... Burch, J. L. (2020a). Extension of the electron diffusion region in a guide field magnetic reconnection at magnetopause. *Astrophys. J.*, *892*(1), L5. https://doi.org/10.3847/2041-8213/

ab7b7c

Zhong, Z. H., Zhou, M., Tang, R. X., Deng, X. H., Turner, D. L., Cohen, I. J., Pang, Y., Man, H. Y., Russell, C. T., ... Burch, J. L. (2020b). Direct evidence for electron acceleration within ion-scale flux rope. *Geophys. Res. Lett.*, *47*(1), e2019GL085141. https://doi.org/10.1029/2019gl085141

Zhong, Z. H., Zhou, M., Deng, X. H., Song, L. J., Graham, D. B., Tang, R. X., Man, H. Y., Pang, Y., Khotyaintsev Yu V., and Giles, B. L. (2021). Three-Dimensional Electron-Scale Magnetic Reconnection in Earth's Magnetosphere. *Geophys. Res. Lett.*, *48*(1), 2020GL090946. https://doi.org/10.1029/2020GL090946

Zhong, Z. H., Zhou, M., Liu, Y. H., Deng, X. H., Tang, R. X., Graham, D. B., Song, L. J., Man, H. Y., Pang, Y., and Khotyaintsev, Y. V. (2022). Stacked electron diffusion regions and electron Kelvin–Helmholtz vortices within the ion diffusion region of collisionless magnetic reconnection. *Astrophys. J. Lett.*, *926*(2), L27. https://doi.org/10.3847/2041-8213/ac4dee

Zhou, M., Deng, X. H., and Huang, S. Y. (2012). Electric field structure inside the secondary island in the reconnection diffusion region. *Phys. Plasmas*, *19*(4), 042902. https://doi.org/10.1063/1.3700194

Zhou, M., Pang, Y., Deng, X. H., Huang, S. Y., and Lai, X. S. (2014). Plasma physics of magnetic island coalescence during magnetic reconnection. *J. Geophys. Res.*: *Space Phys.*, *119*(8), 6177–6189. https://doi.org/10.1002/2013ja019483

Zhou, M., Ashour-Abdalla, M., Deng, X. H., Pang, Y., Fu, H. S., Walker, R., Lapenta, G., Huang, S. Y., Xu, X. J., and Tang, R. X. (2017). Observation of three-dimensional magnetic reconnection in the terrestrial magnetotail. *J. Geophys. Res.*: *Space Phys.*, *122*(9), 9513–9520. https://doi.org/10.1002/2017ja024597

Zhou, M., Deng, X. H., Zhong, Z. H., Pang, Y., Tang, R. X., El-Alaoui, M., Walker, R. J., Russell, C. T., Lapenta, G., ... Lindqvist, P. A. (2019). Observations of an electron diffusion region in symmetric reconnection with weak guide field. *Astrophys. J.*, *870*(1), 34. https://doi.org/10.3847/1538-4357/aaf16f

Zhu, B. J., Yan, H., Yuen, A. D., and Shi, Y. L. (2019). Electron acceleration in interaction of magnetic islands in large temporal-spatial turbulent magnetic reconnection. *Earth and Planetary Physics*, *3*(1), 17–25. https://doi.org/10.26464/epp2019003

Zong, Q-G., and Zhang, H. (2018). *In situ* detection of the electron diffusion region of collisionless magnetic reconnection at the high-latitude magnetopause. *Earth and Planetary Physics*, *2*(3), 231–237. https://doi.org/10.26464/epp2018022